Graphene-based microfluidic perforated microelectrode arrays for retinal electrophysiological studies

Alberto Esteban-Linares,[a,‡] Xiaosi Zhang,[b,‡] Hannah H. Lee,[c] Michael L. Risner,[c] Sharon M. Weiss,[b,d] Ya-Qiong Xu,[b,d] Edward Levine,[c,e,*] and Deyu Li[a,*]

[a]*Department of Mechanical Engineering, Vanderbilt University, Nashville, TN, 37235, United States*
[b]*Department of Electrical and Computer Engineering, Vanderbilt University, Nashville, TN 37235, United States*
[c]*Department of Ophthalmology and Visual Sciences, Vanderbilt Eye Institute, Vanderbilt University Medical Center, Nashville, TN, 37232, United States*
[d]*Department of Physics and Astronomy, Vanderbilt University, Nashville, TN, 37235, United States*
[e]*Department of Cell and Developmental Biology, Vanderbilt University, Nashville, TN 37235, United States*
‡These authors contributed equally to this work.
*Corresponding authors: ed.levine@vumc.org; deyu.li@vanderbilt.edu

Abstract:

Perforated microelectrode arrays (pMEAs) have become essential tools for *ex vivo* retinal electrophysiological studies. pMEAs increase the nutrient supply to the explant and alleviate the accentuated curvature of retina, allowing for long-term culture and intimate contacts between the retina and electrodes for electrophysiological measurements. However, commercial pMEAs are not compatible with *in situ* high-resolution optical imaging and lack the capability of local microenvironment control, which are highly desirable features for relating function to anatomy and probing physiological and pathological mechanisms in retina. Here we report on microfluidic pMEAs (μpMEAs) that combine transparent graphene electrodes and the capability of locally delivering chemical stimulation. We demonstrate the potential of μpMEAs by measuring electrical response of ganglion cells to locally delivered high K^+ stimulation under controlled microenvironments. Importantly, the capability of high-resolution confocal imaging of the retina tissue on top of the graphene electrodes allows for further analyses of the electrical signal source. The new capabilities provided by μpMEAs could allow for retinal electrophysiology assays to address key questions in retinal circuitry studies.

Keywords: microelectrode arrays, microfluidic tissue culture, graphene, retina, electrophysiology.

Introduction

Microelectrode arrays (MEAs) have played a key role in electrophysiological studies of the central nervous system (CNS). For retina, MEAs have been employed to demonstrate physiologic taxonomy and network responses of retinal ganglion cells (RGCs), which project long-range axons from the retina to central targets.[1,2] MEA assays, using whole-mount retinas, provide a format to study RGC circuitry under physiologic and pathologic conditions. For example, electrophysiological studies of RGCs are critical for understanding neurodegeneration related to glaucoma, the world's leading cause of irreversible blindness.[3–5]

For MEA studies of retinal explants, inherent challenges arise due to the dramatic curvature of the tissue that impedes intimate contact to electrodes. This lack of adherence of the retina to the electrode array causes the tissue to move during perfusion, affecting physiologic measurements.[6] These obstacles are usually dealt with by introducing anchors on top of the sample to flatten the retina and maintain placement.[7,8] Unfortunately, slice anchors often limit the nutrient supply and increase the risk of damaging the tissue due to mechanical force.[9,10] Perforated MEAs (pMEAs), with electrodes patterned on a flexible and perforated polyimide substrate placed on top of a suction chamber, use negative pressure through suction to attach the tissue to the electrodes, boosting the signal-to-noise ratio[9,11,12] and improving tissue longevity through better oxygenation. While pMEAs have been mainly used for retina, they have also been used for brain slices to improve nutrient supply to the bottom cell layer and promote tissue survival.[13–16]

While pMEAs have achieved great success, the chemical environment is traditionally modulated by bath perfusion where the media stimulation is applied globally, which precludes local delivery of chemical stimulations such as pharmacological drugs. Local delivery of

reagents is highly desirable in *ex vivo* assays where it is important to control the microenvironment of focalized regions. In fact, focal stimulation has been attempted by releasing small amounts of reagents via glass micropipettes.[17] For instance, Saggere and coworkers have incorporated a multisite chemical delivery system into commercial pMEAs to study the neuromodulation of photoreceptors to restore vision of degenerated retinas.[12,18,19] However, the glass pipette-based delivery system is invasive with pipettes penetrating the tissue from the top and limits the possibility of applying a complex sequence of reagents.[20]

Another limitation of pMEAs is that the relatively large suction chamber prevents *in situ* high-resolution imaging, which can provide crucial information by directly matching physiologic responses to their anatomical origins. Particularly for RGCs, successful imaging could aid in the understanding of glaucoma progression in *ex vivo* models.[21] For instance, intracellular Ca^{2+} was used to monitor the dynamic response of RGCs to acute pressure elevations.[22] Metal MEAs are not suitable for high-resolution imaging, as they are opaque and block the tissue being sensed by the electrode. While transparent electrodes made of PEDOT:PSS,[23,24] ultrathin TiN,[25] and graphene,[26] have been incorporated in various MEA platforms, no report can be found on integrating transparent electrodes in pMEAs that allow for high-resolution imaging.

To further enhance the capability of pMEAs, we report on a graphene electrode-based microfluidic pMEA (μpMEA) platform that is compatible with confocal imaging and local delivery of stimulation reagents. Confocal imaging of THY1.2-YFP retinas is enabled by the incorporation of flexible graphene electrodes, which not only have high optical transparency,[27] but also superior electrical properties[28] and biocompatibility.[29] We demonstrate the potential of this platform by probing the electrophysiologic responses of excised mice retinas under

controlled microenvironments. The μpMEA system could enable novel assays to address unmet needs in neuroscience through multimodal testing and characterization of *ex vivo* tissues.

Experimental Section

Device Design and Assembly

The μpMEA device is composed of a No. 1 coverslip as the substrate, a 100 μm thick polydimethylsiloxane (PDMS) open microfluidic channel layer, a 6.5 μm thick polyimide (PI) layer with patterned graphene electrodes (or Ti/Au for some characterization) and etched through-holes, and a PDMS tubing support layer with inlets and outlets for tubing as well as an open region in the center for retina placement. Figure 1a shows the exploded view of the device components. Each layer is fabricated separately and assembled *via* bonding (see Methods section for fabrication process). Importantly, the μpMEA platform is compatible with high-resolution imaging as the maximum distance from the bottom of the device to the retina is ~246 μm. Also, at 6.5 μm thickness, the PI film is still transparent, allowing for optical imaging. In fact, characterizations have shown that 80% of blue light (450-490 nm) can transmit 6.5 μm PI film.[30] Figure 1b depicts a cross-sectional schematic of the μpMEA with local application of high K^+ stimulation through a delivery channel. As can be seen in the anatomy of the retina, the RGC layer is in contact with the electrodes and holes of the PI layer.

The PDMS open channel layer holds three independent microfluidic channels: two symmetric suction channels to gently attach the retina to the electrodes with negative pressure, which was measured to be 500 ± 100 Pa using a pressure gauge sensor (MPS 1, Elveflow); and a 200 μm wide channel in the middle for localized reagent delivery (Figure S1a). Note that medium is withdrawn from the outlet of the delivery channel to maintain negative pressure, ensuring that only the tissue directly above the delivery channel is stimulated.[31]

The flexible PI film on the PDMS open channel layer serves as the substrate for 16 graphene or Ti/Au (10 nm/100 nm) electrodes with an interelectrode distance (edge-to-edge) of 200 μm to minimize the possibility of recording electrical activity of a cell from multiple electrodes. While graphene electrodes were used to demonstrate full capabilities through high-resolution imaging experiments, Au electrodes were used for initial characterization and chemical stimulation studies due to their easiness to be cleaned for reuse after bioassays. For the transparent electrodes, monolayer graphene grown by chemical vapor deposition was stripped off the Cu substrate by a bubbling transfer method and placed onto the target area of the PI substrate,[32] which was further patterned *via* photolithography and oxygen plasma etching. The Au electrodes are fabricated *via* a lift-off process with electron-beam Au deposition. As explained by Camunas-Mesa et al., the electrode size has a drastic effect on the recording of neuronal spiking,[33] and mid-size electrodes offer an optimal trade-off between low impedance and high signal-to-noise ratio. Based on our observations, electrode dimensions of 30x30 and 40x40 μm^2 for graphene, and 60x60 and 80x80 μm^2 for Au (Figure S1b,c) provided the best trade-off between impedance and signal recording. Evenly distributed holes are fabricated in the sensing region of the PI substrate *via* RIE etching, resulting in a hole-to-surface-area ratio of 27%, which has been shown to provide adequate contact between the retina and substrate.[9] Various through-hole sizes were selected based on previous reports to minimize damage to the retina.[9,16] Lastly, a 1.2 μm thick SU-8 layer is used to passivate the electrode leads.

The PDMS tubing support layer is used for structure stability. This layer holds the retina well, where the tissue sample is positioned, and the tubing for the inlets/outlets of the fluidic circuit in the bottom PDMS layer. The three layers are assembled following a stamp-and-stick bonding technique using a biocompatible epoxy (EPO-TEK 302, Epoxy Technology) as the

gluing material,[34] resulting in an irreversible bond. The fully assembled device is shown in Figure 1c, as well as a zoomed-in view of the sensing region with transparent graphene electrodes (Figure 1d,e), allowing for confocal imaging of the neuronal structures on top of the electrode (Figure 1f).

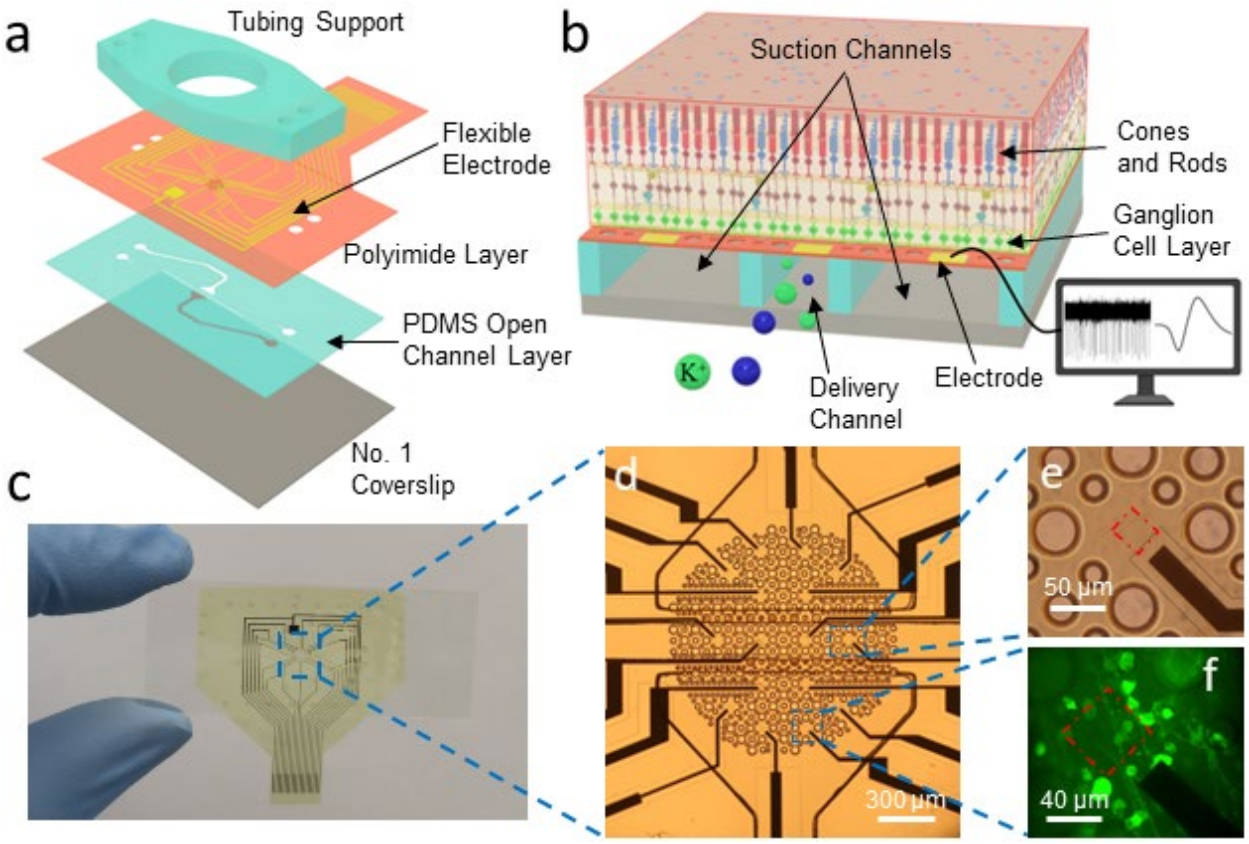

Figure 1. (**a**) Exploded view of the microfluidic-MEA components. The gray plate, blue structures, and red film represent the glass coverslip, PDMS layers, and polyimide layer, respectively. (**b**) A cross-section diagram of µpMEA interfaced with the retina and perforated flexible electrode layer (not drawn to scale). Suction channels are used to bring the retina in contact with the electrodes by applying gentle negative pressure, while the delivery channel is used to locally apply chemical stimulation directly to the ganglion cell layer. Green and blue spheres represent high K^+ and Ames' media, respectively. (**c**) Photograph of the µpMEA device. (**d**) Zoomed-in view of the µpMEA. Top and bottom chambers are the suction channels, whereas the middle section is the delivery channel. (**e,f**) Close-up view of transparent graphene electrode, and maximum projection confocal image of 20 optical sections (0.3 µm steps), indicating the transparency of the graphene probe. Red dashed lines in (**e**) and (**f**) outline the graphene electrode.

The experimental set-up for recording RGC action potentials (APs) is illustrated in Figure 2. In the schematic, the light gray, light blue, and light red colors represent the glass substrate, PDMS and PI layers, respectively. Atop of the retina, a heated cannula (bright red in Figure 2a) is inserted into the retina well to provide heated oxygenated media, and an overflow cannula (dark gray in Figure 2a) is placed at the top of the retina well to prevent media overflow. Black arrows in Figure 2a indicate the induced flow in the delivery channel. Figure 2b shows a photograph of the µpMEA device mounted on the inverted microscope.

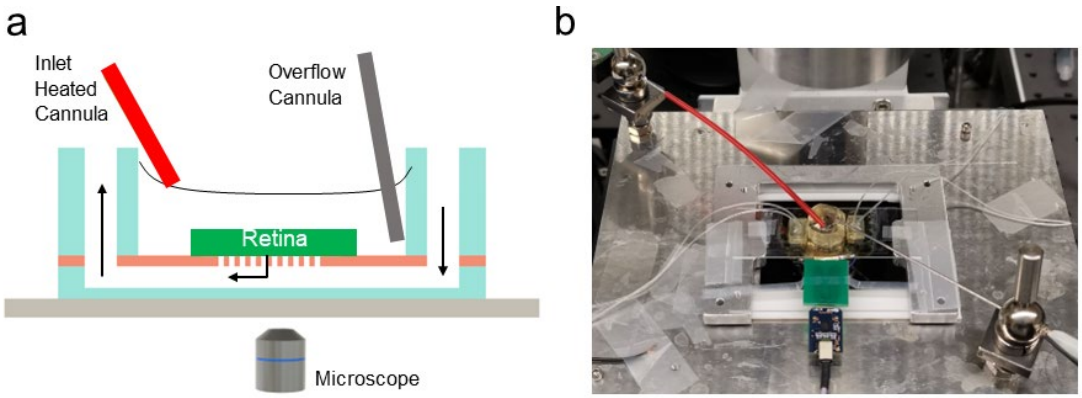

Figure 2: Custom µpMEA set-up. (**a**) Schematic diagram of µpMEA platform where light gray, light blue, and light red represent the glass substrate, PDMS and PI layers, respectively. The green structure denotes the retina. The bright red and dark gray tubing represent the heated inlet and overflow cannulas, respectively. Black arrows illustrate the flow direction. Inverted microscope is located underneath the device. (**b**) Top-view photograph of the µpMEA platform mounted on the inverted epifluorescence microscope with the heated perfusion inlet (red), overflow cannula (metal silver – bottom left), and tubing. The electrical leads on the PI layer are connected to a lab-made printed circuit board zero-insertion-force connector, located at the bottom of the image.

Results and Discussion

Fluidic and Electrical Characterization

First, we tested whether the µpMEAs sensed electrical signals from *ex vivo* retinas comparable to commercial pMEAs (60pMEA, MultiChannel Systems).[12,18,19] To do so, we constructed a simple suction chamber in the 100 µm tall PDMS open channel layer with an

empty center region of 2 mm in diameter connected to a single 400 μm wide suction channel (Figure 3a). The main difference between this device and the commercial pMEA as well as other reported custom platforms is the distance from the PI layer to the bottom of the platform, which exceeds 2 mm in commercial pMEAs, rendering these platforms incompatible with high-resolution imaging.[9,18,26]

Interestingly, we found that all signals detected were from electrodes close to the suction channel (indicated by a white arrow in Figure 3a,b), while no signal could be recorded from the other side of the chamber (Figure 3b,c), which suggested an uneven distribution of the negative pressure in the suction chamber. Moreover, the uneven pressure and attempts to seal the entire chamber with stronger negative pressure proved detrimental to the health and integrity of the retinal tissue, producing tears at multiple locations which are identified by the darker regions in the fluorescence pattern (Figure 3b). This is not an issue in commercial pMEAs because the much larger depth of the suction chamber leads to a rather uniformly distributed negative pressure across the 2 mm diameter region that the holes span. To quantify the distribution of the negative pressure, a three-dimensional computational model was constructed using COMSOL Multiphysics™ (see details in Methods). The simulation results suggest a 122% pressure difference between the holes located closest and furthest from the suction channel (Figure S2a,d) in the 100 μm tall suction chamber in the μpMEA. On the other hand, increasing the chamber height from 100 μm to 1 mm, similar to that in a commercial pMEA, reduced the pressure difference to 3% (Figure S2b,d). To alleviate the uneven pressure distribution across the through-holes while maintaining a channel depth of 100 μm, we added a second suction channel located opposite from the one in Figure 3a, which reduced the pressure difference to 55% (Figure S2c,d). This reduction in the pressure differential was sufficient to ensure an intimate contact across the

entire retina for all the electrodes to be able to sense extracellular Aps and minimize tearing damage.

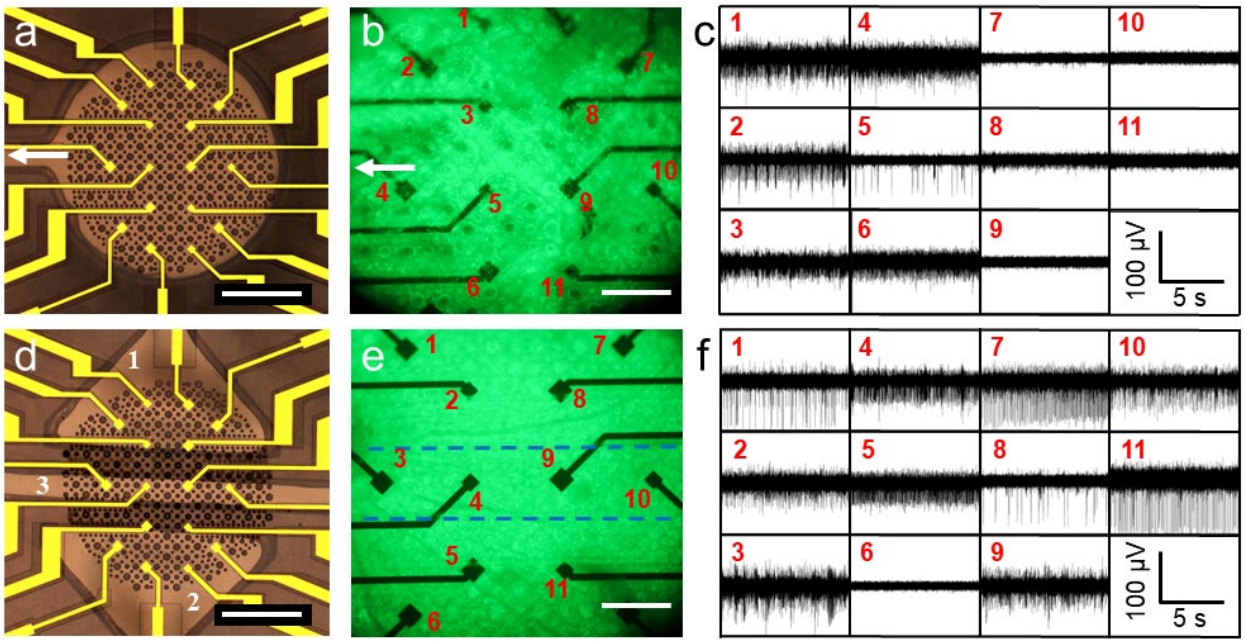

Figure 3. (**a**) Optical image of a one-channel µpMEA device. Scale bar is 500 µm. White arrow indicates the direction of the flow and suction pressure. (**b**) Fluorescence image of the retina placed on the single-channel device where tissue integrity is compromised. White arrow indicates the direction of the flow and suction pressure. Scale bar is 200 µm. (**c**) Spontaneous activity of RGCs sensed by the electrodes numbered in (**b**). The electrodes located closer to the microfluidic channel (white arrow in **b**) detect signal, whereas the ones farther from it do not. (**d**) Optical image of the final version of µpMEA. Top and bottom chambers (1,2) are the suction channels, whereas the middle section is the delivery channel (3). Scale bar is 500 µm. (**e**) Fluorescence image of the retina placed on the final µpMEA device where tissue is healthy. The blue dashed lines indicate the delivery channel. Scale bar is 200 µm. (**f**) Spontaneous activity of RGCs sensed by the electrodes numbered in (**e**). Spiking activity with good signal-to-noise ratio is visible on most electrodes. Note that the data shown in (**b**) and (**f**) is displayed through a 500 Hz high-pass filter for better visualization of spiking activity.

To introduce the capability of delivering local chemical stimulation to the retina, a 200 µm wide channel was added through the center of the suction chamber, dividing the platform into two symmetric regions (Figure 3d – regions 1, 2 and 3 are the suction chambers and the delivery channel, respectively). Four of the 16 electrodes were placed on the microfluidic delivery channel to measure the response of the RGCs that are in direct contact with the reagents flowed

through the delivery channel. As shown in Figure 3e,f, this configuration better stabilizes the retinal structure with much improved tissue integrity, and ensures an intimate contact of the entire retina for most electrodes to be able to sense extracellular APs. In our chemical stimulation experiments, retina was probed for 4 hours by using slight vacuum pressure which allowed tissue morphology to remain intact and APs to be detected with high reliability.

Figure 4a shows the spontaneous firing activity recorded by electrode 1 in Figure 3e before (Suction OFF) and after (Suction ON) suction through the holes was initiated, indicating that negative pressure is essential for reducing the inherent curvature of the retina and consistently obtaining robust recordings of RGC action potentials. When tissue preparation and positioning are adequate, activity can be sensed from most of the electrodes. However, when the retina is folded or is not flat enough on the flexible electrode layer, signals are, in most cases, impossible to measure.

One key factor in this design is that the hydraulic resistance of the delivery microchannel is significantly smaller than the combined hydraulic resistance of the through holes and the porous retinal tissue. This ensured even contact (sealing) of the through holes on top of the delivery channel with retinal tissue. An important consideration is the positioning of the optic-nerve-head (ONH), which is the structure in the posterior ocular part of the retina where RGC axons exit the eye and project through the optic nerve.[35] This aggregate of axon bundles results in an uneven surface,[9] producing poor contact with the nearby electrodes. As depicted in Figure 4b,c, placing the ONH directly on the delivery channel results in poor sealing of the through-holes, causing leakage from the retina well to the delivery channel when performing local stimulation (blue color dye – Figure 4b). Therefore, retinal placement is crucial.

To achieve best fluidic isolation and full seal of the delivery channel, the ONH should be positioned on top of either suction channel distal to the delivery channel. This was demonstrated by flowing and maintaining blue color dye to the delivery channel using negative pressure, as shown in Figure 5a.

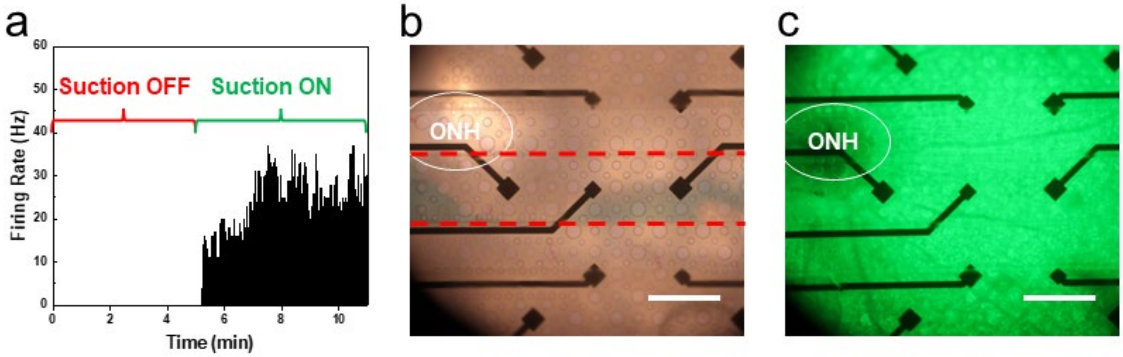

Figure 4. Spontaneous activity sensed by electrode 1 in Figure 3e likely in contact with an RGC body before (suction OFF) and after (suction ON) negative pressure is started at the outlet of the channel. (**b**) Optical image of a retina placed on top of the microfluidic-MEA device where the ONH is placed partially on the delivery channel. This positioning causes leakage and poor sealing of the through-holes due to the non-flat area surrounding the ONH. (**c**) Corresponding fluorescence image to (b). ONH, blood vessels, axons, and RGCs are all visible.

Electrophysiology Characterization

Next, we demonstrate the capability of the μpMEAs to sense RGC electrophysiologic activities in a controlled microenvironment. To showcase the local delivery of pharmacological agents, we tested the response of *ex vivo* retina to extracellular potassium (K^+) stimulation, as this response is well documented.[36,37] Prior to stimulation, the integrity of the tissue was assessed by epifluorescence imaging, and measurements of spontaneous and light-evoked spike activity (Figure S3) with broad-spectrum photopic illumination (tungsten lamp; 3.5 log cd/m^2) in Ames' medium.[26,37] Once stable patterns of spontaneous activity were observed, Ames' medium containing 22 mM K^+ was flowed into the delivery channel (Figure S4 depicts the experimental design) for a duration of 90 s (as depicted by the green shadowed region in Figure 5c).

Afterwards, we discontinued K^+ stimulation and switched to baseline Ames' medium for at least 15 minutes to give the retina enough relaxation time between stimulation sequences. This chemical stimulation scheme was repeated up to three times per retina during the electrophysiological measurements. The cells sensed by the four electrodes located directly on the delivery channel depicted a standard response to high K^+ stimulation (Figure 5c – electrode 1 in Figure 5a), characterized by a sharp increase in the firing rate when the high K^+ medium first reaches the tissue on top of the delivery channel. This induced neuronal depolarization is followed by a depletion period where firing activity ceases due to insufficient ion concentration and inactivation of voltage-gated channels, resulting in depolarization block.[38] Once the high K^+ medium was removed, RGCs entered a refractory period before resuming normal spontaneous activity around the timepoint of 7:30 min.

Figure S5 illustrates the different responses detected by the electrodes located away from the delivery channel with 22 mM K^+ media, which were categorized as strong (a), mild (b), and weak (c), depending on the degree of similarity to a standard response to high K^+, as explained above. Interestingly, a large percentage of electrodes located away from the delivery channel detected strong firing responses, similar to the electrodes located on the delivery channel (Figure 5d - electrode 2 in Figure 5a). This suggested that RGCs responded to high K^+ stimulation even if they were not in direct contact with high K^+ medium. We noted spreading of depolarization block in cells located on electrodes across the entire sensing region, and the response to high K^+ stimulation was not diminished even over 600 μm away from the delivery channel. We only considered strong responses of electrodes off delivery channel (Figure S5a) to be correlated to the ones from electrodes on the delivery channel. To compare the possible correlated activity, the time when firing ceased and resumed were measured (Figure S6). Statistical analysis based on

data collected from 7 recordings of different retinas gave an average time delay of 10.3 ± 5.5 s for ceasing activity between two electrodes located 230 μm apart that are on and off the delivery channel, respectively. Also, the refractory period was, on average, 25.2 seconds shorter for the off-delivery channel electrode as compared to the electrode located on the channel. This is reasonable as the RGCs located off the delivery channel were continuously bathed with baseline Ames' medium and it takes some time for the baseline Ames' to replace the high K^+ medium in the delivery channel.

Gap Junction Contribution to Intercellular RGC Communication

Given the fluidic isolation provided by our device (Figure 5a), we hypothesized that the observed correlated depolarization block induced by high K^+ was mediated by intercellular communication. Consistent with this hypothesis, it has been shown that correlated activity can be orchestrated by a multitude of neuronal and glial processes controlling firing and refractoriness.[39,40] In retina, RGC networks have shown a high level of correlated activity (over 50% of all RGC activity).[41,42] In particular, gap junctions, which regulate correlated firing in RGCs and K^+ buffering among astrocytes,[43–45] were an appealing target to test as the source of correlated depolarization block.

To test the hypothesis that gap junctions mediated the observed correlated depolarization and rule out other possibilities such as potassium diffusion through the porous retina tissue, water-soluble carbenoxolone gap junction blocker (CBX) was applied globally to the retina during local stimulation to temporarily inhibit gap junction mediated signaling (Figure S4 depicts the experimental strategy). Others have shown 50 to 100 μM of CBX eliminates all electrical coupling through gap junctions in retinal circuitry.[46] Therefore, we first identified electrodes

located off the delivery channel with potential correlated responses to those located on the delivery channel. Once the spreading depolarization block occurred, we then examined whether CBX effectively stopped the correlated response to locally delivered K^+. After a recovery period, we switched the global supply to the retina well from baseline Ames' to Ames' mixed with 100 μM of CBX (Figure 5b,e show the case when the retina is bathed with baseline Ames' and Ames' containing 100 μM of CBX, respectively). Then, we repeated the local delivery of high K^+ stimulation as previously described (depicted by the green shadowed region in Figure 5f). Interestingly, the firing pattern sensed by the electrodes on the delivery channel is the same as previously observed when using baseline Ames' as the global bath medium (Figure 5f – electrode 1 in Figure 5a). On the other hand, RGCs sensed by electrodes located off the delivery channel no longer produced correlated responses, and instead, generated spontaneous firing patterns (Figure 5g – electrode 2 in Figure 5a). After seven tests with different retinas, 23 electrodes off the delivery channel detected depolarization block when the global bath was baseline Ames', and only one electrode maintained the same response when CBX was globally applied (Figure 5h). This strongly suggests that the correlated response of neurons located on and off delivery channel when locally stimulated with high K^+ was primarily due to signal transmission through gap junctions.

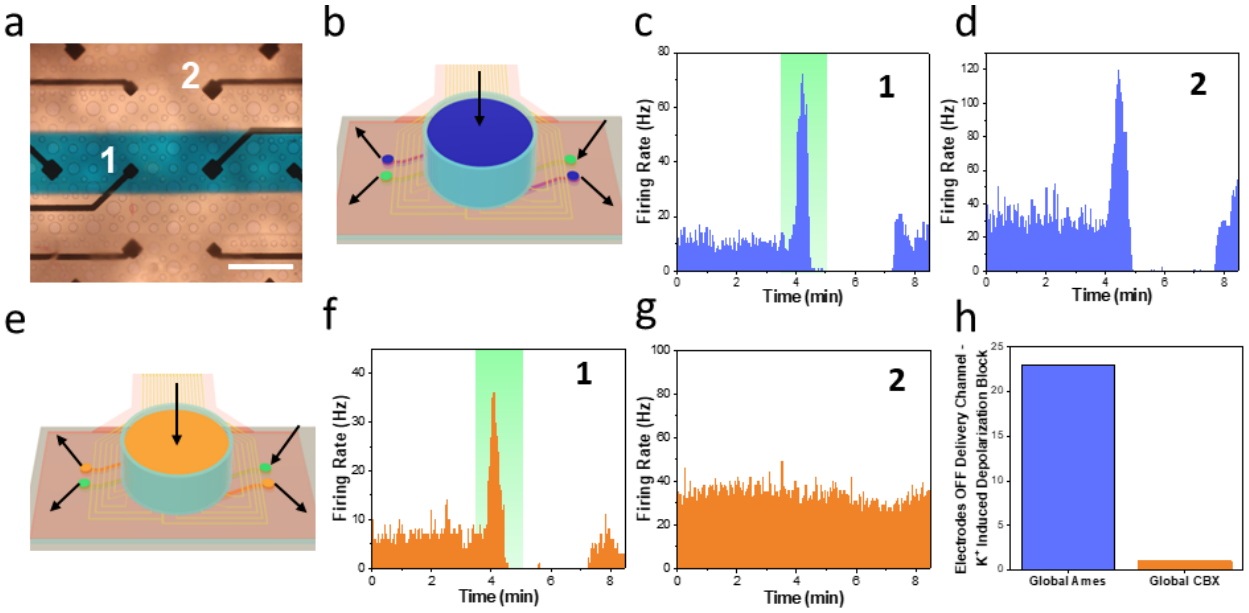

Figure 5. (**a**) Optical image of a retina placed on top of the µpMEA device while delivery of blue color food dye. Scale bar is 200 µm. (b) Schematic diagram showing the retina being globally bathed by Ames' (blue) while high K^+ (green) flows through the delivery channel. Black arrows indicate the flow direction. (**c,d**) Response sensed by electrode 1 and electrode 2 to locally delivered K^+ stimulation during a constant bath of baseline Ames' medium (electrodes shown in **a**). Electrode 2 is 160 µm from the delivery channel. (**e**) Schematic diagram showing the retina being globally bathed by Ames' with 100 µM of CBX (orange) while high K^+ (green) flows through the delivery channel. (**f,g**) Response sensed by electrode 1, and electrode 2 to locally delivered K^+ stimulation during a constant bath of Ames' with 100 µM CBX medium. (**h**) Number of detected APs located off delivery channel that experienced depolarization block due to locally delivered high K^+ stimulation while globally bathed with Ames' (blue) and global CBX (orange).

Spike Waveform Analysis

The spike waveforms detected by an electrode on the delivery channel were also compared during the different global and local stimulations (Figure 6). Upon global high K^+ stimulation, the waveforms grew wider than when globally bathed by Ames' (Figure 6a,b), as previously noted in literature.[37] Interestingly, when the RGCs were locally stimulated through the delivery channel with the same high K^+ medium while being globally bathed by Ames' or CBX, the waveforms did not show significant changes (Figure 6c-f). One possible explanation for the increase in the AP half width during global stimulation with high K^+ is due to the response of

upstream elements of RGC receptive fields (photoreceptors, bipolar cells, etc.). In contrast, during the local delivery of the same chemical, only the nerve fiber and RGC layer are expected to be in contact with the stimulant, while the probed region is still bathed from the top and perfused with Ames' or CBX, which renders a different microenvironment for the RGC receptive fields from the RGC layer.

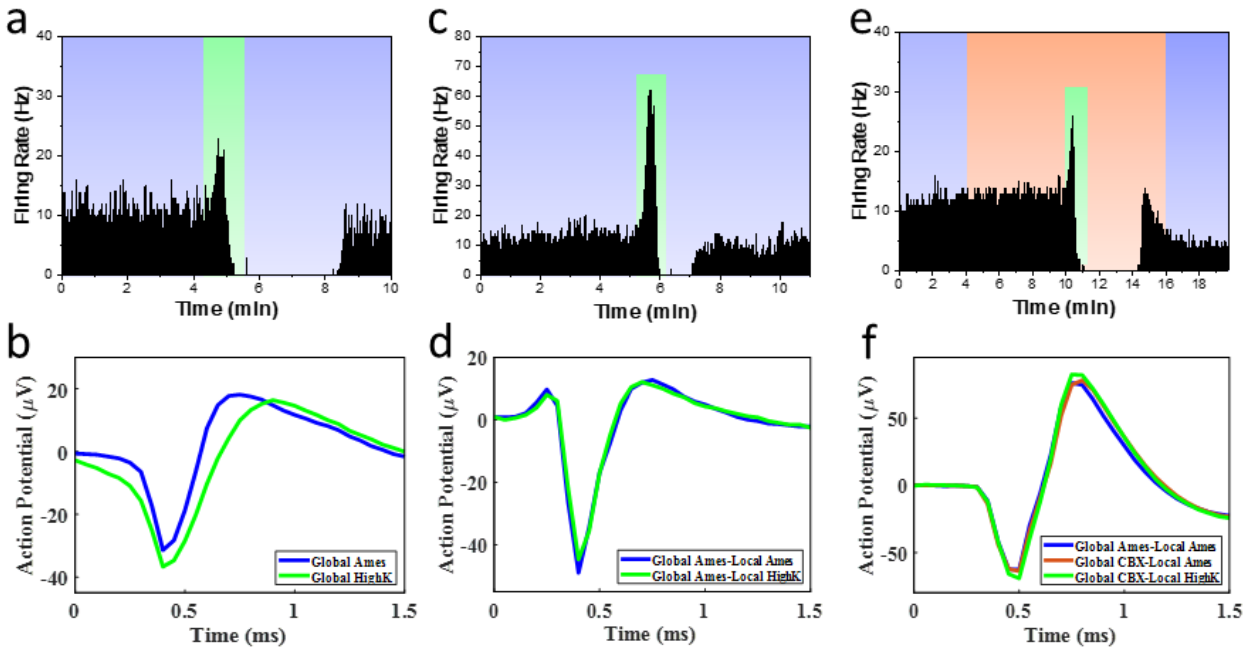

Figure 6. Comparison of AP waveforms of RGCs located on the delivery channel under different stimulations. (**a,b**) Firing rate and AP shapes under global Ames' (blue) and global 22 mM K^+ media (green). (**c,d**) Firing rate and AP shapes under global Ames' (blue) and locally delivered 22 mM K^+ media (green). (**e,f**) Firing rate and AP shapes under global Ames' (blue), global CBX (orange) and locally delivered 22 mM K^+ media (green). The waveforms represent the median waveform of all the spikes detected during the different stimulations in one experiment. The waveforms of 6 RGCs from different experiments were studied for each scenario, depicting similar results.

High-Resolution Imaging Through Graphene Electrodes

Next, we demonstrate the capability of high-resolution imaging through the graphene electrodes. After the electrophysiologic measurements, we performed confocal microscopy of the retina and transparent electrodes to recover the anatomical origins of recorded action potentials. Two examples are depicted in Figure 7. Unambiguous somatic (biphasic) and axonal (triphasic)

spikes were recorded with the graphene electrodes.[47,48] It is known that the waveforms depend on whether the signal is from a cell soma or an axon,[26] whereas the relative amplitude of the signal is closely related to the proximity of the source to the electrode.[7] Figure 7a shows a graphene electrode (edges depicted by white-dashed lines) where an axon bundle and a soma are on top of the probe in close proximity in the vertical direction. Two distinct spikes were sensed by this electrode showing triphasic (Figure 7c) and biphasic (Figure 7d) waveforms. In Figure 7e, several axon bundles and somas are near the graphene probe. However, only biphasic spikes (Figure 7f-h) were recorded by the electrode, which is likely due to retinal deformation. These results clearly show that the graphene-based μpMEA is compatible with *in situ* high-resolution confocal imaging, which should allow for simultaneous electrical and optical measurements of the retina electrophysiological activities.

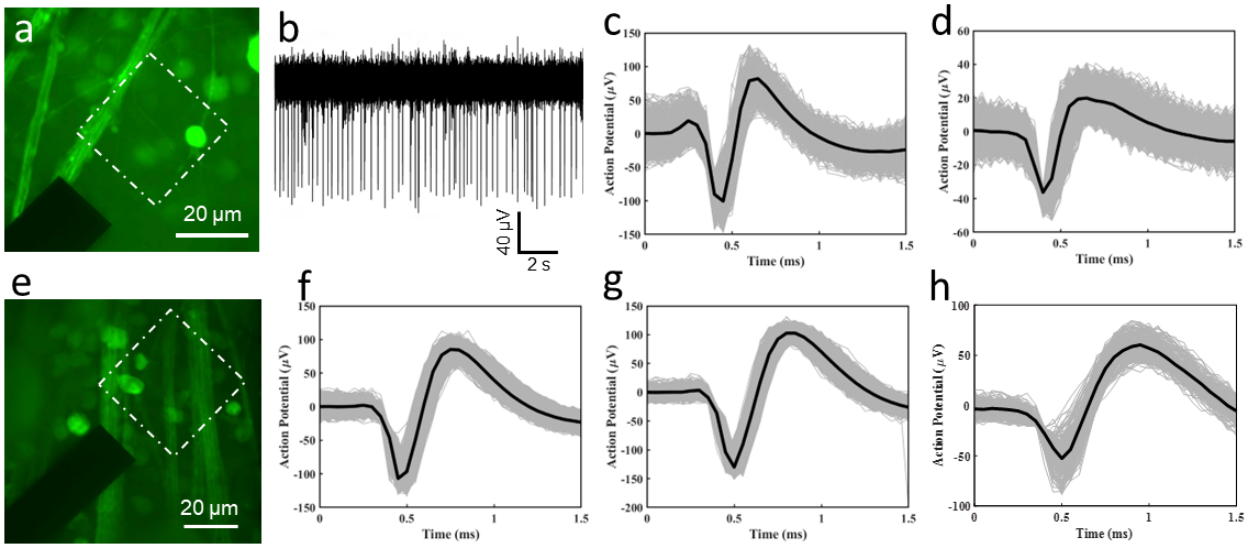

Figure 7. (**a**) Confocal maximum projection image of a graphene electrode in close proximity to an axon bundle and a soma. (**b**) Spontaneous firing activity recorded by the probe with a triphasic (**c**), and biphasic (**d**) waveforms. (**e**) Confocal maximum projection image of a second graphene electrode located near three somas and axon bundles. The graphene probe recorded spontaneous firing activity of three distinct biphasic waveforms (**f**, **g**, **h**).

Conclusion

In summary, we have constructed a graphene electrode-based μpMEA platform with the capability of locally and directly delivering chemical reagents from the bottom fluidic circuit to the axon and RGC layer of the retina. Successful recordings of the electrical activity of the neuronal processes in the retina have been achieved, which showed response to high K^+ stimulation through the delivery channel. We observed correlated responses from electrodes on and off the delivery channel, which was attributed to intercellular communications through gap junctions. High-resolution confocal imaging through the graphene electrodes of the neuronal processes probed during the electrophysiological recording was obtained, which could help to correlate the electrical signals with the neuronal processes. This platform could also be applied for electrophysiological studies of other electroactive tissues such as brain slices, cardiac tissues or 3D cultures, which could benefit from the capability of locally delivering chemical probes through negative pressure to avoid widespread and uncontrolled leakage over tissue. In addition, combining electrical measurements with high-resolution imaging through transparent electrodes could open new avenues of *ex vivo* tissue studies through additional sensing modalities to understand electrophysiological activities of the central nervous system.

Methods

Animal Procurement and Ethics Statement

All experimental procedures involving animals were approved by the Vanderbilt University Institutional Animal Care and Use Committee (IACUC) under protocol M1600235 and align with guidelines of the Association for Research in Vision and Ophthalmology (ARVO) and Association for Accreditation of Laboratory Animal Care (AAALAC). We obtained founder B6.Cg-Tg (Thy1-YFP) 16Jrs/J mice from The Jackson Laboratory (Catalog #003709, Bar Harbor, ME) to establish a colony at the Vanderbilt Division of Animal Care. These mice were

crossed with the female wild-type B6/129 mice and their YFP+ offspring was used for this study. Mice were maintained on a 12-h light cycle and provided food and standard rodent chow as desired. Animals were euthanized approximately 3.5 h following light onset (9:30 AM) by carbon dioxide inhalation until respiration ceased and immediately followed by cervical dislocation.

Retina Preparation

The eyes were excised immediately following cervical dislocation and quickly submerged into gassed (95% O2 and 5% CO2) Ames' medium. Retinas were isolated and dissected under dim red illumination to minimize photopigment bleaching. The retina was then incubated in Ames' medium containing collagenase (241 u/mL, Sigma-Aldrich Corporation) and hyaluronidase (1370 u/mL, Worthington Biochemical Corporation) for 10 min at room temperature. After enzyme treatment, the vitreous body was removed to ensure intimate contact between the retinal ganglion cell layer and electrodes. Finally, the digested retina was washed with Ames' media, mounted photoreceptor side down on Whatman 3MM Chr cellulose paper (Fisher Scientific), and transferred to the MEA device such that the RGC layer was in direct contact with the sensing electrodes.

Device Fabrication

The open channel PDMS layer is fabricated following a modified soft-lithography technique from a master SU-8/Si mold.[49,50] Briefly, after thoroughly cleaning a Si wafer, 100 μm thick SU-8 2050 (MicroChem; Newton, MA) was spun on the wafer and baked before exposure. Then, photolithography was performed using a Karl-Suss Mask Aligner MA6 with 365 nm wavelength light. Finally, the SU-8 structure was baked once more and developed, to finalize the master mold. Before preparing the PDMS, the master mold was silanized by placing it in a desiccator

for 30 min with trichloro (1H,1H,2H,2H-perfluorooctyl) silane (97%, Sigma-Aldrich; Saint Louis, MIS) to decrease the adhesion between the cured PDMS film and the SU-8 structures.[50] The modified soft-lithography technique consisted first in mixing liquid PDMS (SYLGARD 184 Silicone Elastomer Kit, Dow Corning) at a 7.5:1 ratio of pre-polymer to curing agent and poured over the mold. To remove air bubbles entrapped in the mixture, the master was put into a vacuum chamber at room temperature for 30 min. Then, a fluorinated release liner (Scotchpak™ 1022 Release Liner, 3 M) was placed on the SU-8 structure, as well as a 5 mm thick PDMS pad where 4 kg of weight were rested on.[50,51] The sandwiched structure was then cured at 80°C for 3 h. Once cured, the PDMS structure was bonded to a No. 1 glass coverslip *via* oxygen (O_2) plasma treatment and the release liner was peeled off from the PDMS, leaving an open channel device on the coverslip (Figure S1a).

The flexible polyimide (PI) fabrication process starts with spin-coating PI 2611 (HD Microsystems) at 2300 rpm on a clean silicon wafer. After a quick soft-bake at 50°C for 10 min, the wafer was cured in a programmable oven with a nitrogen atmosphere; and the inside temperature was ramped to 300°C at a rate of 4°C/min, where it was held for 3 hr, resulting in a thickness of 6.5 μm. 16 Ti/Au (10/100 nm) electrodes were fabricated following the standard lift-off technique. In order to have an intimate contact between the retina and the platform, the total area of holes should be at least 23% of the total area covered by retina (2 mm).[9] In our design, through-hole diameters span 10, 15, 25, 35, 50 and 60 μm, resulting in a total hole area ratio of 27%. To prepare the holes, a positive photoresist mask SPR220 (SPR 220-7.0 Shipley) was patterned via photolithography. Dry etching of the PI was conducted by combining reactive ion etching and induced coupled plasma (RIE-ICP) with O_2 and CF_4 gas flow using an etcher (Trion Phantom II), resulting in an etch rate of about 1 μm/min.[52] Once the through-holes were fully

etched, the photoresist mask was removed in an acetone bath. 1.2 μm thick SU-8 (SU-8 2002 Microchem) passivation layer was then patterned using photolithography. Figure S1c shows a bright-field image of the PI layer with sixteen 60x60 and 80x80 μm^2 Ti/Au electrodes as well as the etched through-holes and SU-8 passivation layer.

Graphene electrode fabrication followed a similar approach. The metal Ti/Au (10nm/100nm) leads were patterned on PI following the lift-off technique. Through-holes were structured via dry etching with 15 μm thick SPR photoresist as an etching mask. The graphene layer was grown using a standard chemical vapor deposition (CVD) method,[53] and transferred to the PI substrate, using a bubbling transfer method.[32] Lastly, the graphene probes were defined via photolithography and dry etching with O_2 plasma, followed by integrating the SU-8 passivation layer with open graphene windows, outlined by white dashed lines (Figure S1b). The PI film could then be easily peeled off from the silicon wafer using a scalpel and tweezers.

The PDMS tubing support layer provides structure stability to the platform. The total thickness of the PDMS slab is 4 mm. Through-holes were manually punched at the inlets/outlets and at the center region to form the retina chamber with 1.5 mm and 10 mm gage biopsy punchers, respectively.

The three layers were assembled together following a stamp-and-stick bonding technique using a biocompatible epoxy (EPO-TEK 302, Epoxy Technology) as the gluing material.[34] Briefly, components A and B of the epoxy were mixed and spin coated (4000 rpm, 2 min) on a clean silicon wafer, resulting in a bond line 8 μm thick that is transferred to the open channel PDMS layer, and then brought together to the PI layer. The irreversible PDMS-PI bond was

tested through leakage test with a pressure gauge sensor (MPS 1; Elveflow, Paris, France), which yielded an average bonding strength of 350 kPa, similar to a PDMS-glass bond *via* O_2 plasma.[54]

Experimental Set-Up, *Ex vivo* Recordings, and Data Analysis

The μpMEA platform was affixed to the stage of an Olympus IX-81 inverted epifluorescence microscope. Medium temperature was oxygenated and maintained at 36°C by a perfusion inlet. An overflow cannula prevented media overflow. Figure 2 illustrates the electrophysiology set-up on the inverted microscope. The suction and delivery channels are connected to two syringe pumps (11 Elite Pump, Harvard Apparatus) to induce a controllable negative pressure (Figure S4).

The electrical leads of the electrodes were clamped to a lab-made printed circuit board zero-insertion-force connector (green piece in Figure 2b) and connected to a 16-channel amplifier (RHD2132, Intan Technologies). During the experiment, voltage is recorded at a sampling rate of 20 kHz relative to a reference electrode that is in contact with only the conductive media during the recording. Spike sorting was performed, using Plexon Offline Sorter. Butterworth filter was used during analysis followed by thresholding spikes based on their amplitude.

We recovered architecture of THY1.2-YFP retinas in relation to upMEA graphene electrodes using confocal microscopy. We used a Nikon Eclipse Ti inverted microscope with 40x oil-immersion objective equipped with a Yokogawa CSU-X1 spinning disk head. We obtained 0.3 μm serial images in the z direction and created maximum projection images using ImageJ.

COMSOL Simulation

A computational model was developed using COMSOL Multiphysic™ to better understand the pressure distribution across the perforated PI layer. A three-dimensional model, employing

single-phase laminar flow physics was used to simulate the pressure distribution across the holes. For simplicity, the number of holes were reduced from hundreds to 65, with a uniform diameter of 50 μm. Also, the holes were equally distributed in the *x* and *y* directions with a pitch of 180 μm, as shown in Figure S2. A constant atmospheric pressure was applied to the inlet in the retina chamber, while a constant negative pressure that provides a flowrate of 25 μl/min was set at the outlet in the outflow direction, similar to the flowrate used in the experiments. No-slip boundary condition was applied to the entire channel wall and the fluid selected was water with a density of 1000 kg/m^3 and a viscosity of 8.9 x 10^{-4} Pa·s.

Figure S2a,d show the pressure plots and statistical analysis for the one vacuum channel μpMEA with a 100 μm tall chamber, as presented in Figure 3a. Simulation results corroborated our experimental observations, depicting a 122% pressure difference between the holes located closest and furthest from the suction channel. Two other chamber configurations were simulated. First, a one vacuum channel configuration with a 1 mm deep chamber, similar to a commercial pMEA,[9] showed a 3% pressure difference (Figure S2b,d). To alleviate the pressure variation across the through-holes while maintaining a channel depth of 100 μm for high-resolution imagining, a second vacuum channel was added, which was placed at the opposite side from the one in Figure S2a. The addition of the second channel reduced the percentage difference in pressure to 55% (Figure S2c,d).

Light Induced Stimulation of the Retina

In addition to chemical stimulation with high K^+ medium or gap junction blocker CBX, we also performed recording of light-evoked spike activity to investigate the healthiness of the sample. For a detailed explanation of using graphene transparent electrodes to detect direct changes in RGC activity evoked by light stimulation, we refer the reader to Zhang et al.[26] RGC

light responses depend upon their receptive field elements.[55] RGCs are often typified as depolarizing to light increments (ON type), depolarizing to light decrements (OFF type), or depolarizing to both light onset and offset (ON-OFF type).[7,56] During our characterization of the tissue health, we identified the 3 major types of RGCs: ON, OFF, and ON-OFF types under 1 s of white light stimulation, which demonstrated a good response to light stimulation (Figure S3).

µpMEA Set-Up for Gap Junction Blocker Experiment

The strategy to test whether the spread depolarization block is due to locally delivered high K^+ medium is described in Figure S4. Rectangles with black outline borders are the reservoirs containing the different media. Syringe pumps are used to apply a uniform negative pressure (suction) at the outlets of the suction and delivery channels. Gray lines indicate the path of baseline Ames' and gap junction blocker medium from the reservoirs into the µpMEA platform applied globally. Outlets of the suction channels are connected to Syringe Pump 1. Purple lines indicate the path of baseline Ames' and 22 mM K^+ stimulants from the reservoirs into the delivery channel for local delivery. The single outlet of this channel is connected to Syringe Pump 2 to apply a negative pressure to flow in the reagents as well as bind the retina to the electrode substrate. Several gate valves that control the flow from each reservoir are indicated in the diagram as well as a temperature controller.

Time Analysis of Spread of High K^+ Depolarization Block

Figure S6 shows a timeline study where the tissue was locally stimulated by K^+ medium through the delivery channel. The red and green lines depict the depolarization block and recovery detected by the electrodes located ON and OFF the delivery channel, respectively, which correspond to electrodes 1 and 2 of the optical image in Figure 5a. The OFF channel

electrode (electrode 2 in Figure 5a) is 160 μm away from the delivery channel. The correlated response of the electrode off the delivery channel becomes obvious when firing ceases 12.5 seconds after the electrode located on the delivery channel, which is in direct contact with high K^+. After the recovery period, activity reappeared 17.0 seconds earlier on the electrode off the delivery channel. The earlier appearance of firing activity in the OFF electrode can be explained by the continuous perfusion of baseline Ames' medium through the holes in the suction channels. In the delivery channel, baseline Ames' medium is introduced after the stimulation, therefore taking a longer time to reach the tissue.

Author Contributions

Y-Q. X and D. L. conceived the idea. A. E-L., X. Z., M. L. R., E. L., and D. L. designed the experiment; A. E-L., X. Z., H. H. L., and M. L. R. performed the experiments; A. E-L. analyzed the data; S. M. W., Y-Q. X. E. L. and D. L. supervised the project. A. E-L., H. H. L., M. L. R., S. M. W., E. L., and D. L wrote the manuscript.

Conflict of Interest

The authors declare that there are no conflicts of interest.

Acknowledgments

The work carried out in this manuscript was supported by the National Institutes of Health (1R01EY027729), National Science Foundation (EECS#1810088) and BrightFocus Foundation (G2022011S). Biorender was used to prepare Figures.

Notes

Dr. Ya-Qiong Xu is deceased.

References:

(1) Meister, M.; Lagnado, L.; Baylor, D. A. Concerted Signaling by Retinal Ganglion Cells. *Science* **1995**, *270* (5239), 1207–1210. https://doi.org/10.1126/science.270.5239.1207.

(2) Farrow, K.; Masland, R. H. Physiological Clustering of Visual Channels in the Mouse Retina. *J. Neurophysiol.* **2011**, *105* (4), 1516–1530. https://doi.org/10.1152/jn.00331.2010.

(3) Aires, I. D.; Santiago, A. R. Microglial Exosomes in Retinal Neuroinflammation: Focus in Glaucoma. *Neural Regen. Res.* **2021**, *16* (9), 1801–1802. https://doi.org/10.4103/1673-5374.306084.

(4) Qu, J.; Wang, D.; Grosskreutz, C. L. Mechanisms of Retinal Ganglion Cell Injury and Defense in Glaucoma. *Exp. Eye Res.* **2010**, *91* (1), 48–53. https://doi.org/10.1016/j.exer.2010.04.002.

(5) Catalani, E.; Cervia, D. Diabetic Retinopathy: A Matter of Retinal Ganglion Cell Homeostasis. *Neural Regen. Res.* **2020**, *15* (7), 1253–1254. https://doi.org/10.4103/1673-5374.272577.

(6) Henze, D. A.; Borhegyi, Z.; Csicsvari, J.; Mamiya, A.; Harris, K. D.; Buzsáki, G. Intracellular Features Predicted by Extracellular Recordings in the Hippocampus In Vivo. *J. Neurophysiol.* **2000**, *84* (1), 390–400. https://doi.org/10.1152/jn.2000.84.1.390.

(7) Fiscella, M.; Farrow, K.; Jones, I. L.; Jäckel, D.; Müller, J.; Frey, U.; Bakkum, D. J.; Hantz, P.; Roska, B.; Hierlemann, A. Recording from Defined Populations of Retinal Ganglion Cells Using a High-Density CMOS-Integrated Microelectrode Array with Real-Time Switchable Electrode Selection. *J. Neurosci. Methods* **2012**, *211* (1), 103–113. https://doi.org/10.1016/j.jneumeth.2012.08.017.

(8) Ha, Y.; Yoo, H.-J.; Shin, S.; Jun, S. B. Hemispherical Microelectrode Array for Ex Vivo Retinal Neural Recording. *Micromachines* **2020**, *11* (5), 538. https://doi.org/10.3390/mi11050538.

(9) Reinhard, K.; Tikidji-Hamburyan, A.; Seitter, H.; Idrees, S.; Mutter, M.; Benkner, B.; Münch, T. A. Step-By-Step Instructions for Retina Recordings with Perforated Multi Electrode Arrays. *PLOS ONE* **2014**, *9* (8), e106148. https://doi.org/10.1371/journal.pone.0106148.

(10) Marrese, M.; Lonardoni, D.; Boi, F.; van Hoorn, H.; Maccione, A.; Zordan, S.; Iannuzzi, D.; Berdondini, L. Investigating the Effects of Mechanical Stimulation on Retinal Ganglion Cell Spontaneous Spiking Activity. *Front. Neurosci.* **2019**, *13*.

(11) Hanna, L.; Walmsley, L.; Pienaar, A.; Howarth, M.; Brown, T. M. Geniculohypothalamic GABAergic Projections Gate Suprachiasmatic Nucleus Responses to Retinal Input. *J. Physiol.* **2017**, *595* (11), 3621–3649. https://doi.org/10.1113/JP273850.

(12) Inayat, S.; Rountree, C. M.; Troy, J. B.; Saggere, L. Chemical Stimulation of Rat Retinal Neurons: Feasibility of an Epiretinal Neurotransmitter-Based Prosthesis. *J. Neural Eng.* **2014**, *12* (1), 016010. https://doi.org/10.1088/1741-2560/12/1/016010.

(13) Belle, M. D. C.; Baño-Otalora, B.; Piggins, H. D. Perforated Multi-Electrode Array Recording in Hypothalamic Brain Slices. In *Circadian Clocks: Methods and Protocols*; Brown, S. A., Ed.; Methods in Molecular Biology; Springer US: New York, NY, 2021; pp 263–285. https://doi.org/10.1007/978-1-0716-0381-9_20.

(14) Boppart, S. A.; Wheeler, B. C.; Wallace, C. S. A Flexible Perforated Microelectrode Array for Extended Neural Recordings. *IEEE Trans. Biomed. Eng.* **1992**, *39* (1), 37–42. https://doi.org/10.1109/10.108125.

(15) Killian, N. J.; Vernekar, V. N.; Potter, S. M.; Vukasinovic, J. A Device for Long-Term Perfusion, Imaging, and Electrical Interfacing of Brain Tissue In Vitro. *Front. Neurosci.* **2016**, *10*.
(16) Egert, U.; Okujeni, S.; Nisch, W.; Boven, K.-H.; Rudorf, R.; Gottschlich, N.; Stett, A. Perforated Microelectrode Arrays Optimize Oxygen Availability and Signal-to-Noise Ratio in Brain Slice Recordings. *Mikrosystemtechnologie Kongr.* **2005**.
(17) Hunsberger, H. C.; Rudy, C. C.; Batten, S. R.; Gerhardt, G. A.; Reed, M. N. P301L Tau Expression Affects Glutamate Release and Clearance in the Hippocampal Trisynaptic Pathway. *J. Neurochem.* **2015**, *132* (2), 169–182. https://doi.org/10.1111/jnc.12967.
(18) Rountree, C. M.; Raghunathan, A.; Troy, J. B.; Saggere, L. Prototype Chemical Synapse Chip for Spatially Patterned Neurotransmitter Stimulation of the Retina Ex Vivo. *Microsyst. Nanoeng.* **2017**, *3* (1), 1–12. https://doi.org/10.1038/micronano.2017.52.
(19) Rountree, C. M.; Troy, J. B.; Saggere, L. Microfluidics-Based Subretinal Chemical Neuromodulation of Photoreceptor Degenerated Retinas. *Invest. Ophthalmol. Vis. Sci.* **2018**, *59* (1), 418–430. https://doi.org/10.1167/iovs.17-23142.
(20) Scott, A.; Weir, K.; Easton, C.; Huynh, W.; J. Moody, W.; Folch, A. A Microfluidic Microelectrode Array for Simultaneous Electrophysiology, Chemical Stimulation, and Imaging of Brain Slices. *Lab. Chip* **2013**, *13* (4), 527–535. https://doi.org/10.1039/C2LC40826K.
(21) Balendra, S. I.; Normando, E. M.; Bloom, P. A.; Cordeiro, M. F. Advances in Retinal Ganglion Cell Imaging. *Eye* **2015**, *29* (10), 1260–1269. https://doi.org/10.1038/eye.2015.154.
(22) Esteban-Linares, A.; Wareham, L. K.; Walmsley, T. S.; Holden, J. M.; Fitzgerald, M. L.; Pan, Z.; Xu, Y.-Q.; Li, D. Dynamic Observation of Retinal Response to Pressure Elevation in a Microfluidic Chamber. *Anal. Chem.* **2022**, *94* (36), 12297–12304. https://doi.org/10.1021/acs.analchem.1c05652.
(23) Khodagholy, D.; Doublet, T.; Gurfinkel, M.; Quilichini, P.; Ismailova, E.; Leleux, P.; Herve, T.; Sanaur, S.; Bernard, C.; Malliaras, G. G. Highly Conformable Conducting Polymer Electrodes for In Vivo Recordings. *Adv. Mater.* **2011**, *23* (36), H268–H272. https://doi.org/10.1002/adma.201102378.
(24) Susloparova, A.; Halliez, S.; Begard, S.; Colin, M.; Buée, L.; Pecqueur, S.; Alibart, F.; Thomy, V.; Arscott, S.; Pallecchi, E.; Coffinier, Y. Low Impedance and Highly Transparent Microelectrode Arrays (MEA) for in Vitro Neuron Electrical Activity Probing. *Sens. Actuators B Chem.* **2021**, *327*, 128895. https://doi.org/10.1016/j.snb.2020.128895.
(25) Ryynänen, T.; Pelkonen, A.; Grigoras, K.; Ylivaara, O. M. E.; Hyvärinen, T.; Ahopelto, J.; Prunnila, M.; Narkilahti, S.; Lekkala, J. Microelectrode Array With Transparent ALD TiN Electrodes. *Front. Neurosci.* **2019**, *13*.
(26) Zhang, X.; Lee, H.; Zhang, Y.; Walmsley, T. S.; Li, D.; Levine, E.; Xu, Y.-Q. Probing Light-Stimulated Activities in the Retina via Transparent Graphene Electrodes. *ACS Appl. Bio Mater.* **2022**. https://doi.org/10.1021/acsabm.1c01091.
(27) Park, D.-W.; Schendel, A. A.; Mikael, S.; Brodnick, S. K.; Richner, T. J.; Ness, J. P.; Hayat, M. R.; Atry, F.; Frye, S. T.; Pashaie, R.; Thongpang, S.; Ma, Z.; Williams, J. C. Graphene-Based Carbon-Layered Electrode Array Technology for Neural Imaging and Optogenetic Applications. *Nat. Commun.* **2014**, *5* (1), 5258. https://doi.org/10.1038/ncomms6258.

(28) Geim, A. K.; Novoselov, K. S. The Rise of Graphene. *Nat. Mater.* **2007**, *6* (3), 183–191. https://doi.org/10.1038/nmat1849.
(29) Fischer, R. A.; Zhang, Y.; Risner, M. L.; Li, D.; Xu, Y.; Sappington, R. M. Impact of Graphene on the Efficacy of Neuron Culture Substrates. *Adv. Healthc. Mater.* **2018**, *7* (14), 1701290. https://doi.org/10.1002/adhm.201701290.
(30) Brosch, M.; Deckert, M.; Rathi, S.; Takagaki, K.; Weidner, T.; Ohl, F. W.; Schmidt, B.; Lippert, M. T. An Optically Transparent Multi-Electrode Array for Combined Electrophysiology and Optophysiology at the Mesoscopic Scale. *J. Neural Eng.* **2020**, *17* (4), 046014. https://doi.org/10.1088/1741-2552/aba1a4.
(31) Dodson, K. H.; Echevarria, F. D.; Li, D.; Sappington, R. M.; Edd, J. F. Retina-on-a-Chip: A Microfluidic Platform for Point Access Signaling Studies. *Biomed. Microdevices* **2015**, *17* (6), 114. https://doi.org/10.1007/s10544-015-0019-x.
(32) de la Rosa, C. J. L.; Sun, J. (孙捷); Lindvall, N.; Cole, M. T.; Nam, Y.; Löffler, M.; Olsson, E.; Teo, K. B. K. (张谋瑾); Yurgens, A. Frame Assisted H2O Electrolysis Induced H2 Bubbling Transfer of Large Area Graphene Grown by Chemical Vapor Deposition on Cu. *Appl. Phys. Lett.* **2013**, *102* (2), 022101. https://doi.org/10.1063/1.4775583.
(33) Camuñas-Mesa, L. A.; Quiroga, R. Q. A Detailed and Fast Model of Extracellular Recordings. *Neural Comput.* **2013**, *25* (5), 1191–1212. https://doi.org/10.1162/NECO_a_00433.
(34) Wang, S.; Yu, S.; Lu, M.; Zuo, L. Microfabrication of Plastic-PDMS Microfluidic Devices Using Polyimide Release Layer and Selective Adhesive Bonding. *J. Micromechanics Microengineering* **2017**, *27* (5), 055015. https://doi.org/10.1088/1361-6439/aa66ed.
(35) Wang, Y. X.; Panda-Jonas, S.; Jonas, J. B. Optic Nerve Head Anatomy in Myopia and Glaucoma, Including Parapapillary Zones Alpha, Beta, Gamma and Delta: Histology and Clinical Features. *Prog. Retin. Eye Res.* **2021**, *83*, 100933. https://doi.org/10.1016/j.preteyeres.2020.100933.
(36) Tolón, R. M.; Sánchez Franco, F.; de los Frailes, M. T.; Lorenzo, M. J.; Cacicedo, L. Effect of Potassium-Induced Depolarization on Somatostatin Gene Expression in Cultured Fetal Rat Cerebrocortical Cells. *J. Neurosci. Off. J. Soc. Neurosci.* **1994**, *14* (3 Pt 1), 1053–1059.
(37) Boal, A. M.; McGrady, N. R.; Risner, M. L.; Calkins, D. J. Sensitivity to Extracellular Potassium Underlies Type-Intrinsic Differences in Retinal Ganglion Cell Excitability. *Front. Cell. Neurosci.* **2022**, *16*, 966425. https://doi.org/10.3389/fncel.2022.966425.
(38) Cannon, S. C.; Brown, R. H.; Corey, D. P. A Sodium Channel Defect in Hyperkalemic Periodic Paralysis: Potassium-Induced Failure of Inactivation. *Neuron* **1991**, *6* (4), 619–626. https://doi.org/10.1016/0896-6273(91)90064-7.
(39) Zohary, E.; Shadlen, M. N.; Newsome, W. T. Correlated Neuronal Discharge Rate and Its Implications for Psychophysical Performance. *Nature* **1994**, *370* (6485), 140–143. https://doi.org/10.1038/370140a0.
(40) Meister, M.; Berry, M. J. The Neural Code of the Retina. *Neuron* **1999**, *22* (3), 435–450. https://doi.org/10.1016/s0896-6273(00)80700-x.
(41) Völgyi, B.; Pan, F.; Paul, D. L.; Wang, J. T.; Huberman, A. D.; Bloomfield, S. A. Gap Junctions Are Essential for Generating the Correlated Spike Activity of Neighboring

Retinal Ganglion Cells. *PLOS ONE* **2013**, *8* (7), e69426. https://doi.org/10.1371/journal.pone.0069426.
(42) Schnitzer, M. J.; Meister, M. Multineuronal Firing Patterns in the Signal from Eye to Brain. *Neuron* **2003**, *37* (3), 499–511. https://doi.org/10.1016/s0896-6273(03)00004-7.
(43) Völgyi, B.; Kovács-Oller, T.; Atlasz, T.; Wilhelm, M.; Gábriel, R. Gap Junctional Coupling in the Vertebrate Retina: Variations on One Theme? *Prog. Retin. Eye Res.* **2013**, *34*, 1–18. https://doi.org/10.1016/j.preteyeres.2012.12.002.
(44) Volterra, A.; Meldolesi, J. Astrocytes, from Brain Glue to Communication Elements: The Revolution Continues. *Nat. Rev. Neurosci.* **2005**, *6* (8), 626–640. https://doi.org/10.1038/nrn1722.
(45) Neuenschwander, S.; Singer, W. Long-Range Synchronization of Oscillatory Light Responses in the Cat Retina and Lateral Geniculate Nucleus. *Nature* **1996**, *379* (6567), 728–732. https://doi.org/10.1038/379728a0.
(46) Manjarrez-Marmolejo, J.; Franco-Pérez, J. Gap Junction Blockers: An Overview of Their Effects on Induced Seizures in Animal Models. *Curr. Neuropharmacol.* **2016**, *14* (7), 759–771. https://doi.org/10.2174/1570159X14666160603115942.
(47) Rutkove, S. B. Introduction to Volume Conduction. In *The Clinical Neurophysiology Primer*; Blum, A. S., Rutkove, S. B., Eds.; Humana Press: Totowa, NJ, 2007; pp 43–53. https://doi.org/10.1007/978-1-59745-271-7_4.
(48) Vilkhu, R. S.; Madugula, S. S.; Grosberg, L. E.; Gogliettino, A. R.; Hottowy, P.; Dabrowski, W.; Sher, A.; Litke, A. M.; Mitra, S.; Chichilnisky, E. J. Spatially Patterned Bi-Electrode Epiretinal Stimulation for Axon Avoidance at Cellular Resolution. *J. Neural Eng.* **2021**, *18* (6), 066007. https://doi.org/10.1088/1741-2552/ac3450.
(49) Jo, B.-H.; Van Lerberghe, L. M.; Motsegood, K. M.; Beebe, D. J. Three-Dimensional Micro-Channel Fabrication in Polydimethylsiloxane (PDMS) Elastomer. *J. Microelectromechanical Syst.* **2000**, *9* (1), 76–81. https://doi.org/10.1109/84.825780.
(50) Fitzgerald, M. L.; Tsai, S.; Bellan, L. M.; Sappington, R.; Xu, Y.; Li, D. The Relationship between the Young's Modulus and Dry Etching Rate of Polydimethylsiloxane (PDMS). *Biomed. Microdevices* **2019**, *21* (1), 26. https://doi.org/10.1007/s10544-019-0379-8.
(51) Anderson, J. R.; Chiu, D. T.; Jackman, R. J.; Cherniavskaya, O.; McDonald, J. C.; Wu, H.; Whitesides, S. H.; Whitesides, G. M. Fabrication of Topologically Complex Three-Dimensional Microfluidic Systems in PDMS by Rapid Prototyping. *Anal. Chem.* **2000**, *72* (14), 3158–3164. https://doi.org/10.1021/ac9912294.
(52) Turban, G.; Rapeaux, M. Dry Etching of Polyimide in O 2 - CF 4 and O 2 - SF 6 Plasmas. *J. Electrochem. Soc.* **1983**, *130* (11), 2231. https://doi.org/10.1149/1.2119558.
(53) Wang, R.; Shi, M.; Brewer, B.; Yang, L.; Zhang, Y.; Webb, D. J.; Li, D.; Xu, Y.-Q. Ultrasensitive Graphene Optoelectronic Probes for Recording Electrical Activities of Individual Synapses. *Nano Lett.* **2018**, *18* (9), 5702–5708. https://doi.org/10.1021/acs.nanolett.8b02298.
(54) Eddings, M. A.; Johnson, M. A.; Gale, B. K. Determining the Optimal PDMS–PDMS Bonding Technique for Microfluidic Devices. *J. Micromechanics Microengineering* **2008**, *18* (6), 067001. https://doi.org/10.1088/0960-1317/18/6/067001.
(55) He, Q.; Wang, P.; Tian, N. Light-Evoked Synaptic Activity of Retinal Ganglion and Amacrine Cells Is Regulated in Developing Mouse Retina. *Eur. J. Neurosci.* **2011**, *33* (1), 36–48. https://doi.org/10.1111/j.1460-9568.2010.07484.x.

(56) Kim, U. S.; Mahroo, O. A.; Mollon, J. D.; Yu-Wai-Man, P. Retinal Ganglion Cells—Diversity of Cell Types and Clinical Relevance. *Front. Neurol.* **2021**, *12*. https://doi.org/10.3389/fneur.2021.661938.